Dalton Transactions

ROYAL SOCIETY OF CHEMISTRY

PAPER

View Article Online
View Journal | View Issue

Cite this: *Dalton Trans.*, 2022, **51**, 18176

The influence of the Li^+ addition rate during the hydrothermal synthesis of $LiFePO_4$ on the average and local structure†

Michelle Thiebaut, [a,b] Caren Billing, *[a,b] Deena Naidoo [c] and David G. Billing [a,b]

A hydrothermal method was used to synthesize $LiFePO_4$ to explore the effect of the rate of addition of the Li^+ precursor to a mixture of the Fe^{2+} and PO_4^{3-} precursors. Both the average and local structures were investigated using powder X-ray diffraction, Mössbauer spectroscopy and X-ray absorption spectroscopy. Slower addition rates led to increased oxidation of Fe^{2+} to Fe^{3+} despite purging all solutions constantly, as well as increased defects. The local structure as determined by extended X-ray absorption fine structure displayed far less variation between the samples. The formation of a Li_3PO_4 impurity appeared to be independent of the Li^+ addition rate.

Received 4th June 2022,
Accepted 6th October 2022

DOI: 10.1039/d2dt01752k

rsc.li/dalton

Introduction

Lithium iron phosphate ($LiFePO_4$) has been under investigation as a cathode material following the initial insightful work conducted by the Goodenough research group.[1] $LiFePO_4$ has been commercialized and used in electric vehicles such as the Model EV and the Spark from Coda and Chevrolet, respectively.[2,3] This material is attractive due to its thermal stability, high specific capacity, good cyclic stability and excellent cycle life, as well as the low cost and environmentally friendly aspects.[1] Unfortunately it also exhibits low electronic and ionic conductivity at room temperature, where the latter is due to the one dimensional diffusion path of the Li^+ ions (Fig. 1a).[4,5] These drawbacks have been largely overcome by doping on the metal sites to improve ionic conductivity,[6–8] and coating the particles with carbon[8,9] or adding conductive metals to improve electronic conductivity.[10]

The $LiFePO_4$ structure consists of two different octahedral sites, namely, the FeO_6 (M2) site that hosts the Fe^{2+} ion and the LiO_6 (M1) site that hosts the Li^+ ion, as well as a tetrahedral site that hosts PO_4^{3-} [1–55](Fig. 1b).[1] Ideally the iron and lithium atoms are ordered between the M2 and M1 sites, respectively. Oxygen atoms are shared between iron and phosphorus atoms which causes the FeO_6 octahedra to be slightly distorted,[11,12] which is important for the thermal stability of the material.[1,4,13]

$LiFePO_4$ can be synthesized using an array of different methods including solid state, mechano–chemical activation, carbo-thermal treatment, sol–gel, co-precipitation and hydrothermal processes.[14] Syntheses such as solid state, mechano–chemical activation and carbo-thermal treatment produce good crystalline and mostly uniform products, but are time consuming and energy intensive due to the heat treatment steps.[14] Sol–gel and co-precipitation methods produce high purity small particles with increased surface area and decreased Li^+ diffusion distance.[12] A hydrothermal synthetic route, such as the one employed here, reduces cost as well as energy usage due to lower temperatures being utilized. A disadvantage of using lower temperatures is the formation of antisite defects where lithium is replaced by iron on the M1 site which could cause blockages in the one dimensional diffusion channels.[15] Studies, using a co-precipitation route, have shown that an optimal lithium ratio with respect to the other precursors is required. A lithium deficient system could inhibit the formation of $LiFePO_4$ [16] and if $LiFePO_4$ forms, it could negatively affect the electrochemical properties by forming lithium vacancies or the presence of iron on the lithium site.[17] On the other hand, a large excess of lithium readily produced the Li_3PO_4 impurity.[17] By using a $Li:Fe:PO_4$ ratio of 3 : 1 : 1, $LiFePO_4$ is produced and the formation of the Li_3PO_4 impurity is generally suppressed.[16]

In this work a hydrothermal synthesis of $LiFePO_4$ using homemade Teflon bombs, rather than the conventional stain-

[a]*Molecular Science Institute, School of Chemistry, University of the Witwatersrand, Private Bag X3, Johannesburg 2050, South Africa. E-mail: caren.billing@wits.ac.za*
[b]*DST-NRF Centre of Excellence in Strong Materials, University of the Witwatersrand, Private Bag X3, 2050 Johannesburg, South Africa*
[c]*Material Physics Research Institute, School of Physics, University of the Witwatersrand, Private Bag X3, Johannesburg 2050, South Africa*

† Electronic supplementary information (ESI) available. See DOI: https://doi.org/10.1039/d2dt01752k

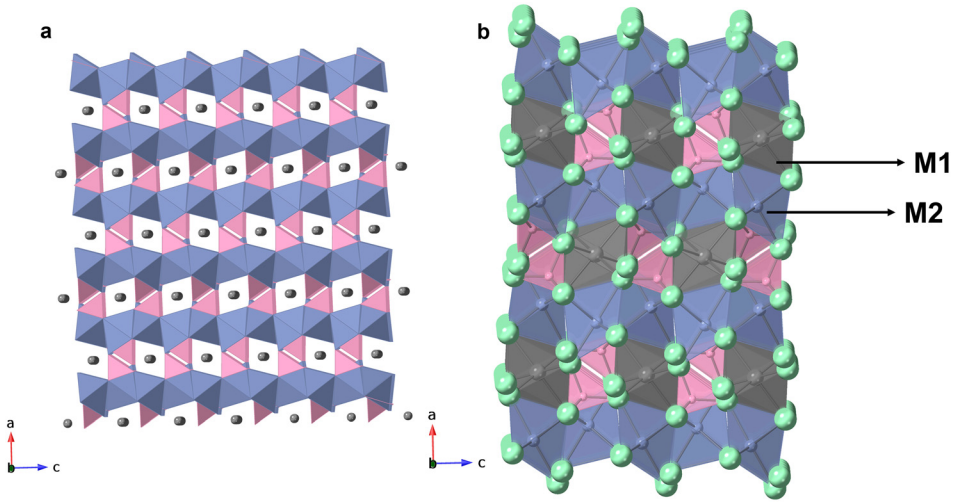

Fig. 1 Crystal structure of $LiFePO_4$. FeO_6 octahedra are represented in blue, PO_4 tetrahedra in pink, Li^+ by the grey spheres or LiO_6 octahedra in grey and the green spheres represents oxygen. (a) The one-dimensional lithium channels are parallel to the *b*-axis. (b) The two octahedral sites, namely the M1 LiO_6 sites and the M2 FeO_6 sites, are indicated.

less steel autoclaves, and adding a threefold excess of lithium as recommended was employed. The dropwise addition of the lithium precursor solution has been suggested by other researchers when synthesizing $LiFePO_4$, but the addition rate has not yet been investigated.[18,19] The effect of the addition rate of the lithium ion precursor to the solution mixture of the Fe^{2+} and phosphate precursors was investigated here and is shown to influence the product obtained to an extent. Of interest was whether a faster addition rate would cause Li_3PO_4 nucleation and hence favour the formation of the Li_3PO_4 impurity, as well as whether a slower addition rate with longer waiting periods between drop additions would increase Fe^{2+} oxidation. Both the average structure (using powder X-ray diffraction (PXRD)) and the local structure around the Fe (using Mössbauer spectroscopy and X-ray absorption spectroscopy (XAS)) were probed. Mössbauer spectroscopy and X-ray absorption near edge structure (XANES) were also used to investigate the oxidation state of Fe, and parameters such as the interatomic distances and the Debye–Waller disorder factors were determined from extended X-ray absorption fine structure (EXAFS).

Experimental

$LiFePO_4$ was synthesised in homemade Teflon bombs (Fig. S1†) with a total volume of 18.5 mL using a hydrothermal synthetic route. The precursors used were LiOH (98%, Sigma Aldrich), $FeSO_4{\cdot}7H_2O$ (99%, Sigma Aldrich) and 85 wt% H_3PO_4 (Merck). Deionised water (Milli-Q, 18 MΩ cm) which was purged with nitrogen was used to make all solutions. A 1.2 M LiOH solution was added dropwise to a $FeSO_4/H_3PO_4$ aqueous mixture ensuring a 3 : 1 : 1 $Li : Fe : PO_4$ molar ratio. Purging and stirring of the solutions were carried out throughout the synthesis to reduce the oxidation of Fe^{2+} to Fe^{3+} and to ensure proper mixing of the precursors, respectively. The addition rate of the LiOH solution to the $FeSO_4/H_3PO_4$ solution was varied by adding one drop every 1, 3, 4 and 5 seconds using a glass Pasteur pipette and a rubber bulb (the samples produced are thus referred to as 1 s, 3 s, 4 s and 5 s, respectively). In general, it took ~1 minute for all the solution to be added for the 1 s addition rate, and likewise it took ~5 minutes for the 5 s addition rate. Once addition was complete for each sample, the mixture was thoroughly mixed and purged for another five minutes before transferring it to the Teflon bomb, which had also been flushed with nitrogen to remove air from the empty vessels. The solution occupied 25% of the total volume of the bomb. The bombs were sealed and placed in an oven for 48 hours at 120 °C, following this they were removed from the oven and left to cool to room temperature. The samples were filtered and washed 4–5 times with deionised water before being placed in the oven to dry at 60 °C for 1 day and then ground using an agate mortar and pestle.

PXRD

Powder X-ray diffraction data were collected at room temperature for all samples which were loaded in Kapton capillaries at the 28-ID-1 beamline of the National Synchrotron Light Source II (NSLS-II) at Brookhaven National Laboratory (BNL), New York. Phases were identified using the software DIFFRAC. SUITE EVA version 4.2.1.10 that is linked to the crystallography open database (COD).[20] Jedit 4.3.1. was used to construct the structure files and Rietveld refinement was performed using Bruker AXS TOPAS version 5 [21] over a 2theta range of 1.7–8.5°. The simple axial divergence model[22] was used to described the asymmetry due to divergence and the peak shape was described using the Thompson–Cox–Hastings Pseudo-Voight function (TCHZ).[23] The NIST 660c (LaB_6) standard was used to determine the X-ray wavelength (0.167057(4) Å) in the refinements and a 4th order Chebychev polynomial function was

employed to describe the background scattering. The starting structure used in the refinements was the $LiFePO_4$ structure resolved by Streltsov *et al.*[24] The refined structural parameters were the scale factor, lattice parameters, the occupancy of iron and lithium, isotropic thermal displacement, fractional coordinates and both Gaussian and Lorentzian strain.

Mössbauer spectroscopy

A ^{57}Co γ-ray source (30 mCi) and a multichannel analyser was utilised to record the transmission mode Mössbauer spectra at room temperature. The isomer shift and velocity was calibrated using an α-Fe foil and Vinda[25] (version 0.7) in Microsoft Excel was used to perform the analysis by fitting a sum of Voigt doublets. A Voigt model was chosen to describe the line shape due to the possible presence of a range of Fe environments. The line widths were used to account for slight variations due to disorder and were constrained to a minimum value of 0.265 mm s^{-1} as per the calibration. Discrete doublets were used as a way to prevent overfitting of the data. Research conducted by Amisse *et al.*[18] and Li and Shinno[26] were used to identify the major Fe environments.

XAS

Fe K-edge X-ray absorption spectra were collected at the B18 beamline at the Diamond Light Source (DLS), Oxfordshire, United Kingdom. The storage ring energy was 3 eV with a top-up mode at nominal current of 300 mA. The monochromator crystal was [Si(111)] and the mirrors were coated with Pt. Harmonic rejection mirrors were also utilised. All measurements were made in transmission mode. The first ionization chamber was filled with nitrogen and the second and third ionization chambers were filled with argon. The reference materials that were used to compare the oxidation state and geometry of the Fe in the XANES region were $LiFePO_4$ (>97%, Sigma Aldrich), $FePO_4{\cdot}4H_2O$ (97%, Sigma Aldrich) and α-Fe_2O_3 (puriss, Riedel-de Haën). Pellets of the samples and reference materials were prepared by grinding and mixing with cellulose (Avicel PH-101, Sigma Aldrich) before being pressed into 13 mm pellets sizes at 1.5 ton. The energy calibration was done at the synchrotron using an Fe foil as an internal reference with the collection of three scans for each pellet. The scans were aligned and merged using the reference channel and the scan of the $LiFePO_4$ reference material. The background was removed and normalized with the R_{bkg} = 1, indicating all values below 1 would be considered as part of the background. Strong spline clamps were used at higher energies. Athena[27] was used for data processing and XANES analysis and Artemis[27] was used for the EXAFS analysis. The multiple peak fitting tool in Origin8 (2016) was used to fit a Lorentzian function to the peaks and to determine the peak positions and intensities.

Results and discussion

Powder X-ray diffraction

To fully understand and characterize the effects of the Li^+ addition rate on the average structure of the product, PXRD with Rietveld refinements was used. From the analyses the lattice parameters, occupancies on the M2 and M1 sites and the interatomic distances were determined. The refinements of the XRD data for the samples with varied lithium addition rates are shown in Fig. 2a–d. Full Rietveld refinement data can be found in the ESI under sections 2 and 3.† The peak intensities for the 4 s and 5 s samples were lower than that for the 1 s and 3 s samples indicating a decreased extent of crystallinity. This was also confirmed by the noisier difference curve in Fig. 2c and d, also an indication of the decrease in the crystallinity. For the 1 s and 4 s samples only $LiFePO_4$ (*Pnma*, #62) was detected whereas the 3 s sample contained a small percentage (1.85%) of Li_3PO_4, a common impurity in $LiFePO_4$,[28] and the 5 s sample had a much higher Li_3PO_4 content (19.17%). The 5 s sample also had an unidentified impurity phase present as indicated in Fig. 2d. The structural information of $LiFePO_4$ extracted from the refinements are summarized in Table 1.

The lattice parameters (Table 1) for all the samples were very similar indicating that the presence of Li_3PO_4 or the unidentified impurity phase present did not affect these parameters. The unit cell volume for the 4 s and 5 s samples is similar (~291 Å) which is most likely due to an increased amount of defects present in these samples.[18] The presence of some Fe^{3+} on the M2 site (and possibly some Fe on the M1 site could also be Fe^{3+}) would cause a decrease in the unit cell parameters since there is the replacement of the larger Fe^{2+} (0.78 Å) (and possibly Li^+ (0.76 Å)) with the smaller Fe^{3+} (0.645 Å) in the octahedral environment.[29] This is usually observed with doping when Fe^{2+} is replaced with a metal ion with a smaller ionic radius.[28,30] Overall, the unit cell volumes for the samples are similar to the ideal and reported unit cell volume of 291.3 $Å^3$.[18,31]

The occupancies for both the M2 (Fe^{2+}) and M1 (Li^+) sites were refined. To determine if Li^+ was also present on the M2 site, Li^+ was included in the refinement at the same fractional coordinates as that of Fe, however, this led to high occupancy errors indicating the presence of vacancies rather than Li^+ on the M2 site (Table 1). The presence of vacancies on the M2 site implies that in order to maintain charge neutrality, Fe^{3+} replaced some of the Fe^{2+} in the structure.[32] The 5 s sample had the lowest percentage of Fe on the M2 site, closely followed by the 4 s sample, and thus again implying possibly the highest percentage of Fe^{3+} present in the structure. The M1 site was occupied by Li^+ as well as partially by Fe (Table 1), with the 1 s and 3 s samples having similar and the lowest Fe occupancies and the 5 s sample having the highest percentage of Fe occupying this site. Since Fe replaced Li^+ on the M1 site but no Li^+ replaced Fe on the M2 site, it implies that these are antisite defects and not site-exchange defects.[33] Chen *et al.*[15] reported a 7% occupancy of Fe on the Li^+ site for samples synthesized *via* the hydrothermal method when also using a synthesis temperature of 120 °C. In their case an autoclave was used where better temperature control can be implemented. This may be an indication that the temperature inside the Teflon bombs used here did not quite reach 120 °C.

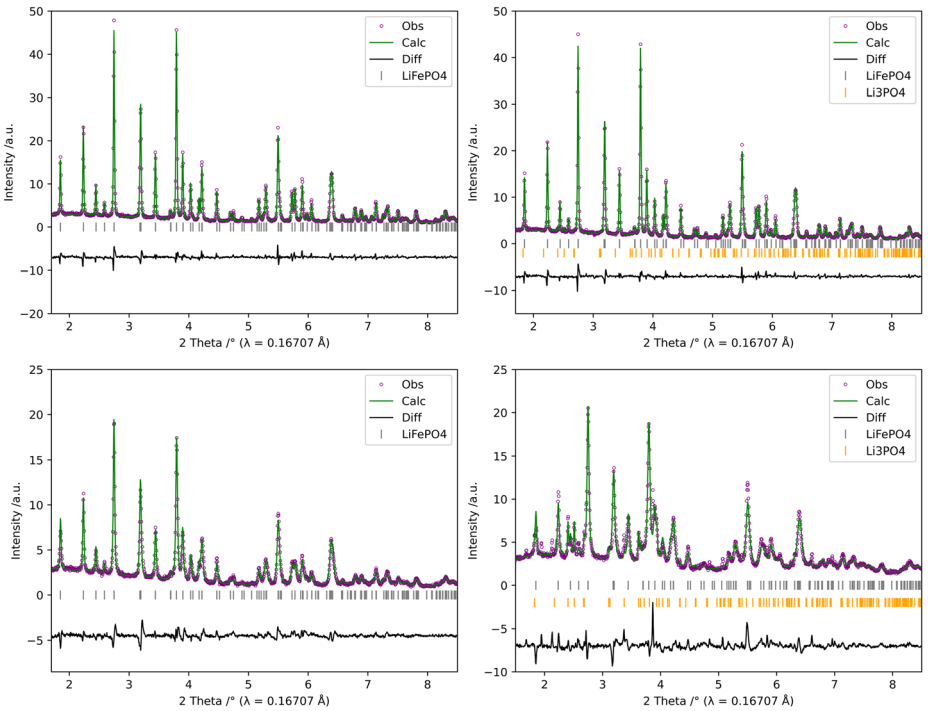

Fig. 2 Rietveld refinement plots of the XRD data of the (a) 1 s, (b) 3 s, (c) 4 s and (d) 5 s $LiFePO_4$ samples showing the observed (purple), calculated (green) and difference (black) plots. Bragg reflections for $LiFePO_4$ and Li_3PO_4 are indicated with the grey and yellow markers, respectively. Peaks due to some unidentified impurity in the 5 s sample are indicated by (*).(a–d)

Table 1 The refined structural parameters for $LiFePO_4$, including the lattice parameters (a, b and c), volume and site occupancies for each sample

Sample	*a*/Å	*b*/Å	*c*/Å	Volume/Å^3	Fe_{occ} (M2)/%	Li^+_{occ} (M1)/%	Fe_{occ} (M1)/%
1 s	10.349(3)	5.9940(2)	4.7066(1)	291.97(2)	99.13(7)	91.14(3)	8.9(3)
3 s	10.349(3)	5.9947(2)	4.7064(1)	291.99(2)	99.03(5)	91.18(3)	8.81(7)
4 s	10.329(8)	5.9899(5)	4.7022(4)	290.92(4)	96.3(2)	89.89(9)	10.11(9)
5 s	10.34(2)	5.989(1)	4.6995(9)	291.13(9)	95.3(2)	83.1(2)	16.9(1)

The FeO_6 octahedra in the $LiFePO_4$ structure displayed four distinct interatomic interactions as shown in Table 2 where Fe–O(1) and Fe–O(2) correspond to the axial positions and the four Fe–O(3) interactions are in the equatorial positions.[11,24]

The average Fe–O (M2–O) interatomic distance can also be used to predict the presence of Fe^{3+} (Table 2) since the average interatomic distance for Fe^{2+}–O in an octahedral structure is ideally between 2.157–2.172 Å (ref. 31, 34 and 35) and for Fe^{3+}–O it is between 2.015–2.045 Å.[31,35] The results in Table 2 show that the average Fe–O distance in all four samples (in the range 2.093–2.136 Å) were shorter than the ideal Fe^{2+}–O distance implying that partial oxidation of Fe^{2+} to Fe^{3+} had occurred. This shows that the 4 s and 5 s samples contained the largest amount of Fe^{3+} which correlates with the higher number of vacancies on the M2 site (Table 1). The interatomic distance for the 5 s sample is also the closest to that for Fe^{3+}–O indicating that Fe^{2+} had been oxidized to a larger extent for this sample.

Table 2 The M2–O (Fe–O) interatomic distances (in Å) for each sample

	1 s	3 s	4 s	5 s
Fe–O(1)	2.187	2.194	2.131	2.068
Fe–O(2)	2.057	2.056	2.009	1.994
Fe–O(3) × 2	2.041	2.042	2.004	1.967
Fe–O(3) × 2	2.238	2.240	2.266	2.280
Average Fe–O	2.134	2.136	2.113	2.093

The bond valence sums (BVS) were also used to more qualitatively determine the average oxidation state of Fe for each sample using the average Fe–O distance in Table S2† (see section 4 in the ESI†). The BVS was found to be 2.07 and 2.09 for the 1 s and 3 s samples, respectively. For the 4 s and 5 s samples the BVS was found to be 2.22 and 2.34, respectively, clearly indicating a higher Fe^{3+} content and especially so for the 5 s sample.

Mössbauer spectroscopy

Mössbauer spectroscopy was used to provide information regarding the local environment and the oxidation states of Fe

on the M2 and M1 sites. The different Fe environments and the percentage of each environment were examined for each sample, thereby giving an indication of the extent of disorder. Different Voigt doublets were used to fit the measured data and five different Fe environments (referred to as D1–D5) were identified in the 1 s, 3 s and 4 s samples. Mössbauer spectroscopy was not performed on the 5 s sample due to the poor quality of the product. The Mössbauer spectra in Fig. 3 are deconvoluted to show the extent to which each Fe environment contributes to each spectrum. The χ^2 values ranged between 1.04 and 1.43 (summarized in Table S8 of the ESI† together with the Vinda plots in Fig. S7–S9†). The isomer shift (δ) and quadrupole splitting (ΔE_Q) were used to determine the different environments. D1, D2 and D3 are Fe^{2+} environments and D4 and D5 are Fe^{3+} environments. Both D1 and D2 were identified as Fe^{2+} on the M2 site in $LiFePO_4$; D1 as the normal distorted Fe^{2+} on the M2 site (δ = 1.22–1.23 mm s^{-1} and ΔE_Q = 2.94–2.95 mm s^{-1})[18,36,37] and D2 is assigned to a more distorted octahedral environment (δ = 1.21 mm s^{-1} and ΔE_Q = 2.64 mm s^{-1}) as established by the decrease in ΔE_Q.[18] D2 was reported by Amisse *et al.*[18] as a more distorted Fe^{2+} environment, but has not been referred to in other literature. D3 was identified as Fe^{2+} on the M1 site that replaced some of the Li^+ (δ = 1.20 mm s^{-1} and ΔE_Q = 1.74 mm s^{-1}).[26] D4 was identified as Fe^{3+} occupying the M1 (Li^+) site in $LiFePO_4$ (δ = 0.43–0.45 mm s^{-1} and ΔE_Q = 0.70–0.76 mm s^{-1})[18,36,37] and D5 was identified as Fe^{3+} on the M2 site where Fe^{2+} was replaced by Fe^{3+} (δ = 0.45 mm s^{-1} and ΔE_Q = 0.95–1.13 mm s^{-1}).[18,37] D4 and D5 are not always distinguishable as two different environments and are most commonly referred to only as single a source of Fe^{3+}.[36,38] In the $LiFePO_4$ samples analyzed here, D1 and D5 were the most common environments detected.

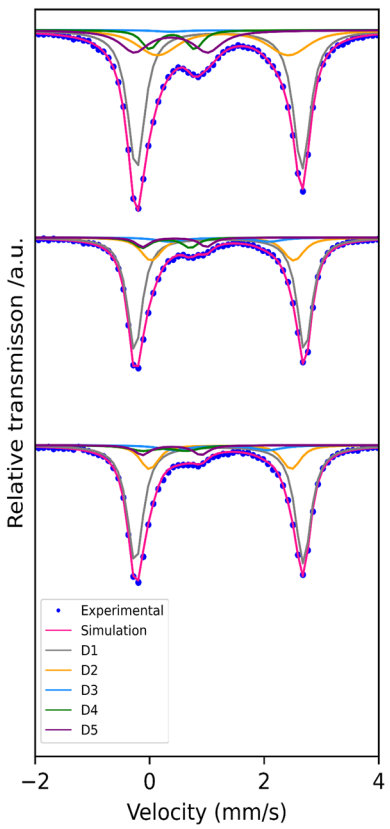

Fig. 3 Mössbauer spectra of (from the bottom to the top) the 1 s, 3 s and 4 s Li^+ addition rate $LiFePO_4$ samples showing the different Fe environments present. D1–D5 represents the different doublets used to described the different environments.

The isomer shifts, quadrupole splitting and the line width, better known as full width at half maximum (Γ), for each environment for the samples are summarized in Table 3 and the percentage contribution from each environment is summarized in Table 4.

The total Fe content as Fe^{2+} in the 1 s, 3 s and 4 s samples is 89%, 89% and 78%, respectively, with the remainder present as Fe^{3+}. The higher Fe^{3+} content in the 4 s sample was also evident from the increase in the shouldering compared to that observed for the 1 s and 3 s samples. Additionally, the higher Fe^{3+} content on the M2 site confirms conclusions drawn from the XRD results predicting higher Fe^{3+} content from the increased percentage vacancies (Table 1) and the shorter Fe–O interatomic distances (Table 2). Most of the Fe^{2+} is in the less distorted D1 environment on the M2 site and the 4 s sample had the highest percentage of Fe^{2+} in the more disordered D2 environment.

The presence of D4 confirmed that some of the Fe on the M1 site is Fe^{3+}, as suggested by XRD results in Table 1. Contrary to the findings from XRD, Mössbauer spectroscopy detected more Fe on the M1 site for the 1 s and 3 s samples as compared to

Table 3 Hyperfine parameters obtained from the analysis of the Mössbauer spectra, including the full width at half maximum (Γ) for each Fe environment. All parameters are given in terms of mm s^{-1}

Environment	Parameter	1 s	3 s	4 s
D1–Fe(II) (M2)	δ	1.22(1)	1.23(1)	1.21(1)
	ΔE_Q	2.93(1)	2.96(1)	2.89(1)
	Γ	0.32(1)	0.30(1)	0.33(1)
D2–Fe(II) (M2)	δ	1.23(1)	1.26(1)	1.28(1)
	ΔE_Q	2.47(1)	2.46(1)	2.29(1)
	Γ	0.28(1)	0.34(1)	0.60(1)
D3–Fe(II) (M1)	δ	1.25(2)	1.22(3)	1.23(3)
	ΔE_Q	1.64(4)	1.74(5)	1.74(4)
	Γ	0.60(4)	0.56(2)	0.60(1)
D4–Fe(II) (M1)	δ	0.26(1)	0.28(1)	0.39(1)
	ΔE_Q	0.76(2)	0.77(1)	0.79(1)
	Γ	0.56(4)	0.31(1)	0.28(1)
D5–Fe(II) (M2)	δ	0.38(1)	0.30(1)	0.37(1)
	ΔE_Q	1.02(1)	1.04(1)	1.28(1)
	Γ	0.32(1)	0.28(1)	0.59(1)

Table 4 The area contribution (%) of each environment

	D1–Fe(II) (M2)	D2–Fe(II) (M2)	D3–Fe(II) (M1)	D4–Fe(III) (M1)	D5–Fe(III) (M2)
1 s	68(8)	15(3)	6(1)	5(1)	6(1)
3 s	67(8)	17(2)	5(1)	6(1)	5(1)
4 s	56(8)	21(3)	1(1)	7(1)	15(3)

that for the 4 s sample which could indicate some amorphous material present that could not be detected by XRD. Another explanation could be that there are vacancies on the M1 site since the occupancies on this site were determined by refinement but assuming the site is fully occupied by either lithium or iron. The percentage contribution from D5 (Table 4) is significantly higher than that expected from XRD results, pointing to a possible Fe^{3+}-containing amorphous phase not detected by XRD.

The line width (Γ) was refined to account for varying extents of disorder in the different environments; this parameter has not always been considered when studying $LiFePO_4$ and the effects of broadening on a more distorted environment has not been reported previously. The full width at half maximum for Fe in a discrete and undistorted octahedral environment is expected to be 0.2–0.3 mm s^{-1}.[36,37] The D3 environment shows the highest disorder across all the samples (Table 3). The D2 and D5 environments for the 4 s sample showed a large extent of disorder which is not surprising based on the range of Fe–O interatomic distances for this sample found by XRD (Table 2). Interestingly the D4 environment for the 1 s sample was also more distorted.

X-ray absorption spectroscopy

From the analysis of the Fe K-edge XAS data, information can be inferred on the local environment (such as changes in the oxidation state, the geometry and the distortion) and the local structure around the Fe atom. Both the XANES region (which incorporates the pre-edge, rising absorption edge and main edge) and EXAFS oscillations of normalized XAS spectra of the synthesized $LiFePO_4$ samples were scrutinized.

The sharing of oxygen atoms between the iron and phosphorus in $LiFePO_4$ (Fig. 1b) causes a reduction in the symmetry around iron from O_h to C_s by breaking the inversion centre and mixing of the 3d–4p orbitals. This lower symmetry produces a crystal-field splitting of the 3d states into two energy levels.[13] The 1s → 3d transition thus becomes partially dipole allowed and the presence of two weak peaks[39] can be observed in the pre-edge region.[11,40–42] The corresponding peaks appear at ~7112 eV (t_{2g}) and ~7114 eV (e_g).[11,13] The position of these peaks can be used to identify differences in the oxidation state, with peaks at higher energy reflecting more Fe^{3+} than Fe^{2+}, and the intensity of these peaks indicate differences in the geometry around Fe, with greater distortion causing an increase in intensity.[11,13,39,43,44]

Reference materials are generally used to characterise and compare features in the XANES region to that of the samples under investigation and here $LiFePO_4$, $FePO_4{\cdot}4H_2O$ and α-Fe_2O_3 were employed. Enlarged regions of the pre-edge and main edge are shown in Fig. 4 and the peak positions and intensities for the three reference materials and the four samples are summarized in Table 5. A more complete characterization of the $LiFePO_4$ reference material was also done and is given in section 7 of the Supporting Information. The $FePO_4{\cdot}4H_2O$ and α-Fe_2O_3 reference materials which contain Fe^{3+} gave peaks at higher energies as expected.[11,45] The more prominent pre-edge feature observed for α-Fe_2O_3 at 7115.2 eV signifies a greater extent of distortion around the Fe^{3+} as compared to that of $FePO_4{\cdot}4H_2O$.[11,40,46] The similar intensities of the e_g peak of $LiFePO_4$ and the peak of $FePO_4{\cdot}4H_2O$ indicates a similarity in the structure and distortion.

The t_{2g} and e_g peaks are present in the spectra for all four synthesized samples (Fig. 4a and Table 5), all having very similar peak positions. The slight deviations to higher energies are most likely due to the presence of Fe^{3+} in the octahedral site as noted in the analyses by XRD (Table 1) for all the samples, and Mössbauer spectroscopy (Tables 3 and 4) for the 1 s, 3 s and 4 s samples. The differences in the intensity of the t_{2g} and e_g peaks for the samples could imply differences in the distortion around the axes in the t_{2g} and e_g positions or any changes in the Fe^{3+} content (Table 5). These different octahedral environments and changes in Fe^{3+} content are clearly evident in the Mössbauer spectroscopy data. The 4 s and 5 s samples produced the lowest intensity t_{2g} peak and an increased intensity in the e_g peak, especially for the 5 s sample, as compared to the peaks for the 1 s and 3 s samples as well as the reference sample. This could be caused by the higher Fe^{3+} content resulting in a slightly different crystal field splitting and could be moving to a structure more similar to that of the $FePO_4{\cdot}4H_2O$ reference material.

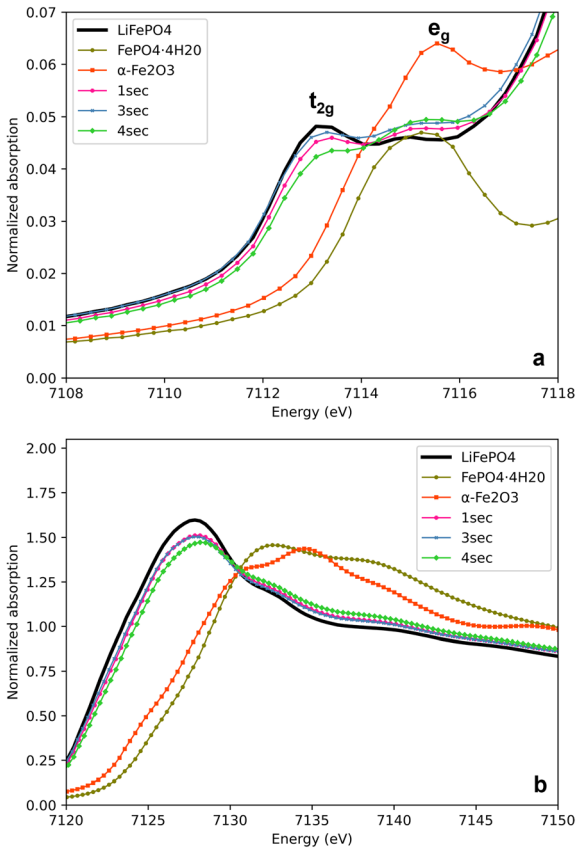

Fig. 4 Comparison of Fe K-edge XANES (a) pre-edge and (b) main edge region of the different reference materials and the three samples. The t_{2g} and e_g peaks are indicated in (a).

Table 5 Comparison of the pre-edge and main edge peak positions and intensities for the reference materials and samples

	Pre-edge t_{2g} peak		Pre-edge e_g peak		Main edge peak	
Sample	Position/eV	Intensity/au	Position/eV	Intensity/au	Position/eV	Intensity/au
$LiFePO_4$	7112.9	0.0480	7115.2	0.0457	7127.8	1.59
$FePO_4{\cdot}4H_2O$	—	—	7115.7	0.0469	7133.0	1.46
α-Fe_2O_3	—	—	7115.2	0.0642	7134.3	2.44
1 s	7113.2	0.0452	7115.6	0.0477	7127.9	1.52
3 s	7113.0	0.0469	7115.6	0.0488	7217.9	1.50
4 s	7113.8	0.0423	7115.6	0.0494	7128.3	1.47
5 s	7113.2	0.0427	7115.5	0.0537	7128.5	1.39

The rising absorption edge and the main edge correspond to the 1s → 4p and 1s → continuum transitions, respectively.[13,47,48] The main edge is usually at a position of ~7126 eV for $LiFePO_4$.[49] The positions of both the rising and main absorption edge can be used to determine the oxidation state of Fe where the higher oxidation state (*i.e.* Fe^{3+}) would give a peak at higher energy.[11,43,50]

There is a slight shift to higher energy in the rising absorption edge for the samples as compared to that for the $LiFePO_4$ reference material, and more so for the 4 s and 5 s samples (Fig. 4b) which is also reflected in the peak positions of the main edge. The larger shift for these samples clearly indicates a higher Fe^{3+} content and the identical positions for the 1 s and 3 s samples imply these two samples have very similar Fe^{2+} content. These observations confirm the results obtained from the interatomic distances by XRD (Table 2) and Mössbauer spectroscopy (Table 4).

Data in the EXAFS region were used to probe the local structure of the reference material and the three samples. The Fourier transformed spectra were phase corrected and a k^3-Hanning window was used for the three sets. The same starting model used for the XRD refinements (Streltsov *et al.*[24]) was used to calculate the initial scattering paths. The cluster size used for the scattering path calculation was 7.038 Å and only paths up to 5.0 Å were included. Two different models were considered for the change in the interatomic distance (ΔR). For both models the amplitude reduction factor ($S_0{}^2$) and the energy shift (ΔE_0) were kept as the same refineable parameter for all the scattering paths, the Debye–Waller disorder factors (σ^2) were unique for every scattering path and all parameters were allowed to refine throughout the refinement. For the first model ΔR was allowed to be unique for every scattering path, however, this led to high σ^2 errors. To obtain reasonable σ^2 errors the octahedra of the first coordination shell had to remain undistorted, *i.e.* with six of the same Fe–O interatomic distances. Since results from both XRD and Mössbauer spectroscopy data indicated the clear presence of distorted octahedra another model was rather considered. For the second model ΔR was only allowed to be unique for every coordination shell rather than every scattering path. This model led to reasonable σ^2 errors, small residual factors and distorted octahedra, and was therefore used for all the refinements.

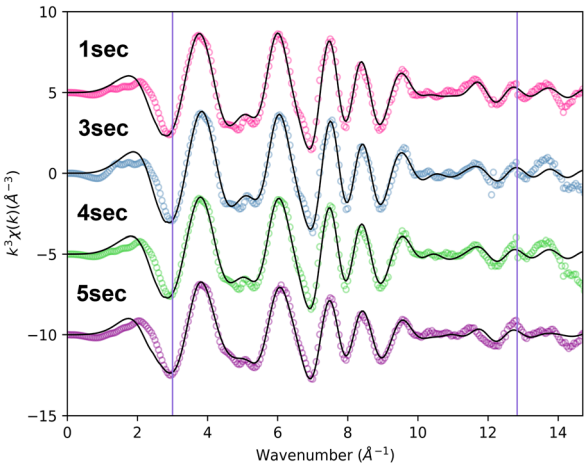

Fig. 5 Comparison of the Fe k^3-weighted $[k^3\chi(k)]$ fits for the different Li^+ addition rate samples.

The fitted $[k^3\chi(k)]$ function obtained using FEFF6[51,52] and employing a fitting range of 3–12.828 $Å^{-1}$ is given in Fig. 5. The radial structure functions together with the Fourier transform (FT) of the real space were fitted over 1.3–5 Å (Fig. 6a–d). The extracted data of the synthesised samples and the $LiFePO_4$ reference material are summarised in Table 6 and include the coordination shells, interatomic distances (where 1, 2 and 3 refer to the different Fe–O distances) and Debye–Waller factors which indicate the extent of disorder. Values for $S_0{}^2$, ΔE_0 and the *R*-factors for each sample are given in Table S9 in the ESI.† From this data the scattering processes around the absorbing atom (Fe) can be identified. The first scattering process corresponds to the first and most prominent peak in Fig. 6a–d and was identified as oxygen (using the interatomic distances and the input file) in an octahedral arrangement around Fe.[11,13,53] This is consistent with the $LiFePO_4$ structure,[11,13,24] the XRD and Mössbauer spectroscopy results. From EXAFS modelling, two different Fe–O interatomic distances were identified rather than the four determined using XRD (Table 2). The long Fe–O interatomic distances (Table 6) were longer than that determined when using XRD, and the short Fe–O interatomic distances were shorter. The average distance determined using XAS were

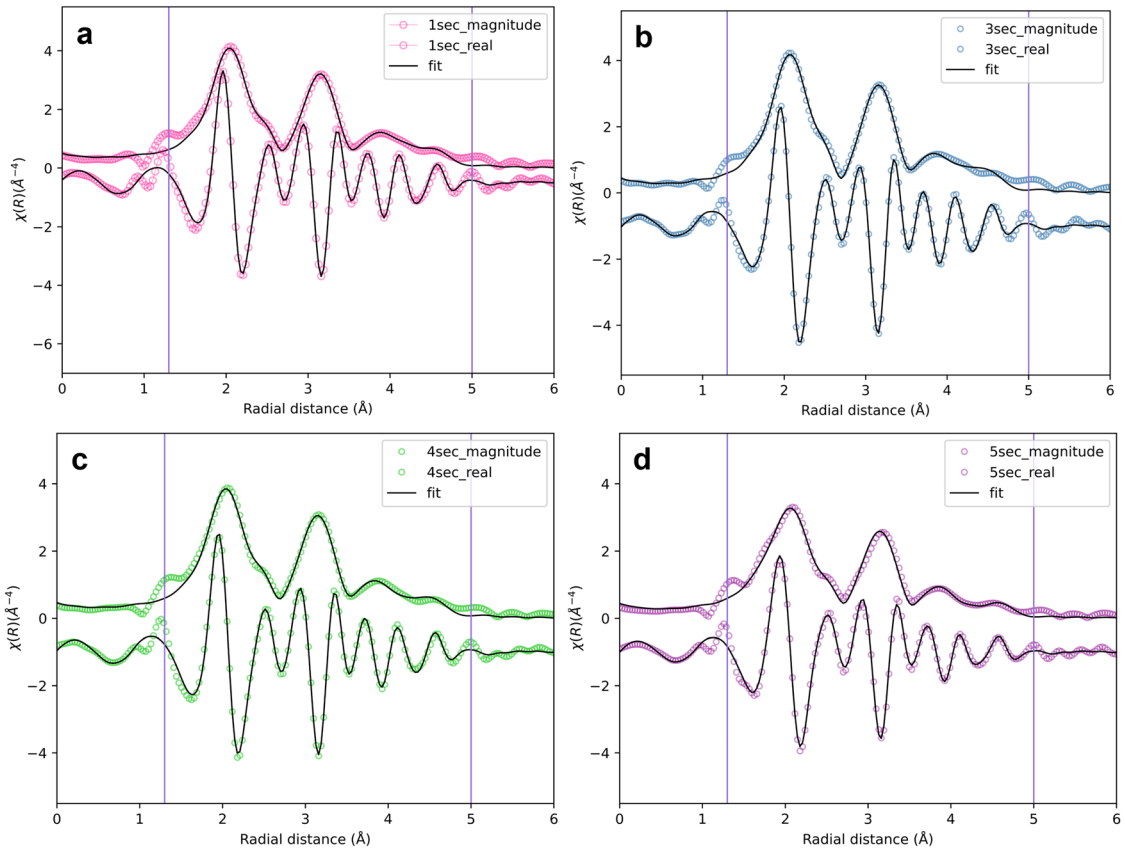

Fig. 6 Comparison of the Fe k^3-weighted [$k^3\chi(k)$] fits for the different Li^+ addition rate samples. The experimental FT magnitude (top) and FT real (bottom) of the EXAFS $k^3\chi(k)$ data and the theoretical FEFF fit (black) of the (a) 1 s, (b) 3 s, (c) 4 s and (d) 5 s $LiFePO_4$ samples. The fitting window is indicated by the vertical lines.

shorter for the 3 s and 4 s sample. The average of the shortest interatomic distances as determined from XRD is comparable to the shorter interatomic distance determined here. The second scattering process was identified as the phosphorus coordination shell and with a coordination number of five.[11,13] The third scattering process was identified as the iron coordination shell with a coordination number of four.[11,13] The interatomic of the $LiFePO_4$ reference material for the Fe–O and Fe–Fe coordination shells is comparable to that for the 1 s, 3 s and 4 s samples, but greater variation was noticed for the 5 s sample. Interestingly the interatomic distances of the $LiFePO_4$ reference material and the 5 s sample for the Fe–P coordination shell is more comparable. The Debye–Waller factors for the $LiFePO_4$ reference material are smaller than for the synthesized samples indicating the reference sample has a better ordered structure.

The average interatomic distances (Table 7) are essentially the same for the 1 s, 3 s and 4 s samples for the different coordination shells. The 5 s sample exhibited shorter Fe–O (due to the increase in Fe^{3+} content) and longer Fe–P and Fe–Fe distances than the other samples. The third coordination shell produces a much weaker signal compared to that of the first and second shell and also consists of multiple scattering process.[54] This makes it more difficult to extract reliable structural information and causes parameters for this shell to appear to be less sensitive to differences such as the oxidation state of Fe between samples.

Data from the various techniques used here have clearly pointed to the 4 s and 5 s samples having more Fe^{3+} present than the other two samples, but a difference is only apparent in the Fe–Fe distances for the 5 s sample.

The average Fe–O interatomic distance is only slightly shorter than those reported in other EXAFS studies[11,13,53] (Table 7) which could result from a higher Fe^{3+} content, but unfortunately the Fe^{3+} content was not recorded in these studies. More significant differences were found for the Fe–P and Fe–Fe distances where the former were shorter and the latter longer than that in literature. The disorder as determined in this work is larger than that found in similar EXAFS studies (Table 7).[11,13,53] The disorder determined for the reference material is similar to that of the synthesized samples except for the disorder for the Fe–Fe coordination shell which was within the reported range. The greater disorder in the samples could arise from (i) some disorder in the cation distribution between the M1 and M2 sites[55] as indicated from the analysis of the Mössbauer spectroscopy data (Tables 3 and 4)

Table 6 Structural parameters from the $[k^3\chi(k)]$ and radial structure function determined using FEFF for the first, second and third coordination shell of the Li^+ addition rate samples

Sample	Shell	Coordination number	Interatomic distance/Å	Debye–Waller factor/Å^2
$LiFePO_4$ reference material	Fe–O1	3	2.15(2)	0.011(4)
	Fe–O2	3	2.06(2)	0.008(2)
	Fe–P	1	2.83(1)	0.008(3)
	Fe–P	4	3.25(1)	0.007(1)
	Fe–Fe	2	3.83(1)	0.007(2)
	Fe–Fe	2	4.65(1)	0.008(3)
1 s	Fe–O1	2	2.21(1)	0.013(5)
	Fe–O3	4	2.07(1)	0.010(1)
	Fe–P	2	2.835(7)	0.012(1)
	Fe–P	3	3.259(7)	0.007(1)
	Fe–Fe	2	3.84(1)	0.011(2)
	Fe–Fe	2	4.66(1)	0.013(4)
3 s	Fe–O2	4	2.12(1)	0.020(5)
	Fe–O3	2	2.08(1)	0.009(2)
	Fe–P	2	2.836(7)	0.014(2)
	Fe–P	3	3.261(7)	0.007(1)
	Fe–Fe	2	3.83(1)	0.011(2)
	Fe–Fe	2	4.65(1)	0.015(6)
4 s	Fe–O1	2	2.20(1)	0.015(6)
	Fe–O3	4	2.06(1)	0.011(1)
	Fe–P	2	2.835(7)	0.013(1)
	Fe–P	3	3.260(7)	0.007(1)
	Fe–Fe	2	3.83(1)	0.011(1)
	Fe–Fe	2	4.65(1)	0.015(4)
5 s	Fe–O2	1	2.09(9)	0.008(4)
	Fe–O1	5	2.05(9)	0.017(3)
	Fe–P	1	2.817(6)	0.009(2)
	Fe–P	4	3.241(6)	0.0089(9)
	Fe–Fe	1	3.81(1)	0.011(4)
	Fe–Fe	3	4.64(2)	0.017(3)

Table 7 The average interatomic distances and average Debye–Waller disorder factors for this work as well as from work done by Haas *et al.*,[13] Deb *et al.*[11] and Hsu *et al.*[53]

Shell	Sample	Average interatomic distance/Å	Average interatomic distance/Å (ref. 11, 13 and 53)	Average Debye–Waller disorder factor/Å^2	Average Debye–Waller disorder factor/Å^2 (ref. 11, 13 and 53)
Fe–O	$LiFePO_4$	2.12	2.13–2.15	0.010	0.0028–0.0082
	1 s	2.11		0.010	
	3 s	2.11		0.020	
	4 s	2.11		0.010	
	5 s	2.06		0.016	
Fe–P	$LiFePO_4$	3.17	3.15–3.25	0.007	0.0045–0.0049
	1 s	3.09		0.009	
	3 s	3.09		0.010	
	4 s	3.09		0.009	
	5 s	3.16		0.009	
Fe–Fe	$LiFePO_4$	4.24	3.94–4.00	0.007	0.0054–0.0096
	1 s	4.25		0.012	
	3 s	4.24		0.013	
	4 s	4.24		0.013	
	5 s	4.43		0.016	

and (ii) the presence of Fe^{3+} in the samples. The information extracted from EXAFS show no differences in the local structure between the different samples unlike the structure information determined from XRD and Mössbauer results.

Conclusions

The effect of the addition rate of the Li^+ precursor solution to the mixture of the Fe^{2+} and PO_4^{3-} precursors when using a low

temperature hydrothermal method to synthesize $LiFePO_4$ was investigated. The effect on both the average and local structures of the resulting product (for the 1 s, 3 s, 4 s and 5 s samples) were considered to determine if there was an optimum addition rate. The 1 s and 3 s samples showed many similarities, including the occupancies on the M2 and M1 sites, the interatomic bond distances, and the Fe^{2+} and Fe^{3+} content. The 4 s and particularly the 5 s samples showed less promising results with a higher percentage of defects present on the M2 and M1 sites. The Fe^{3+} content in the 4 s sample, as determined from Mössbauer spectroscopy, was about double the amount present in the 1 s and 3 s samples. Even though this analysis was not run for the 5 s sample, it was clear from all other analyses that the Fe^{3+} content was even higher than that in the 4 s sample. The pre-edge region showed a decrease in intensity of the t_{2g} peak and an enhancement of the e_g peak, likely due to the increase in Fe^{3+} content. The EXAFS results showed only slight variation between samples (except for the 5 s sample) and the local structure remained essentially the same for the different samples (again, except for the 5 s sample). Compared to the local structure, the average structure showed a lot more variability between the samples.

It is evident that for faster Li^+ addition rates (adding one drop of solution between every 1–3 s) less Fe^{2+} to Fe^{3+} oxidation occurred and there were fewer defects in the structure. The extent of oxidation then increased with slower addition rates which corresponds to an increased duration of addition. The formation of Li_3PO_4 does not appear to be dependent on the Li^+ addition rate, with 1.85% detected in the 3 s sample and 19.17% in the 5 s sample. This also shows that contrary to the initial hypothesis, Li_3PO_4 formation is not promoted by faster addition rates. From this work it is clear that the Li^+ addition rate of one drop every 1–3 s, using solutions with the specified concentrations and nitrogen purging, was optimal. The presence of Fe^{3+} on the M1 site and the presence of Fe^{3+} in all samples, however, could still negatively affect the electrochemical performance. Synthesising pure $LiFePO_4$ with minimal defects is important for optimising the cathode material's electrochemical performance, especially when defects and impurities obstruct the Li^+ movement in the one-dimensional channel. By understanding the effects of various steps in the synthetic process, such as the Li^+ addition rate looked at here, more insight can be gained on how to improve the methodology to ensure defect and impurity formation is kept to a minimum.

Conflicts of interest

There are no conflicts to declare.

Acknowledgements

The authors would like to thank the UKRI-GCRF START programme (Diamond Light Source, United Kingdom), National Research Foundation (NRF, South Africa) and Department of Science and Innovation (DSI, South Africa) as well as the University of the Witwatersrand and the Materials for Energy Research Group (MERG) for their financial support. Additional thanks is extended to Brookhaven National Laboratory, USA (beamline 28-ID-1 (PDF) at NSLS II) and the Energy Materials Block Allocation Group SP14239 (beamline B18 Core-XAS at Diamond Light Source). The authors would also like to acknowledge the assistance from Dan Olds at BNL, Alan Chadwick and Giannantonio Cibin at DLS, and Gerrard Peters and Rudolph Erasmus from the School of Physics for their assistance in collecting data, as well as David Pickup from the University of Kent for his assistance in the analysis of the XAS data.

Notes and references

1 A. K. Padhi, K. S. Nanjundaswamy and J. B. Goodenough, *J. Electrochem. Soc.*, 1997, **144**, 1188.
2 M. Anderman, *Technical report: Assessing the Future of Hybrid and Electric Vehicles: The 2014 xEV Industry Insider Report, Advanced Automotive Batteries*, 2013, **https://www.ehcar.net/library/rapport/rapport022.pdf**.
3 G. E. Blomgren, *J. Electrochem. Soc.*, 2017, **164**, A5019–A5025.
4 A. K. Padhi, K. S. Nanjundaswamy, C. Masquelier, S. Okada and J. B. Goodenough, *J. Electrochem. Soc.*, 1997, **144**, 1609–1613.
5 M. S. Whittingham, *Chem. Rev.*, 2004, **104**, 4271–4301.
6 J. Xu and G. Chen, *Physica B: Condens. Matter*, 2010, **405**, 803–807.
7 Z. Xu, L. Gao, Y. Liu and L. Li, *J. Electrochem. Soc.*, 2016, **163**, A2600–A2610.
8 H. Zhang, Y. Xu, C. Zhao, X. Yang and Q. Jiang, *Electrochim. Acta*, 2012, **83**, 341–347.
9 P. P. Prosini, D. Zane and M. Pasquali, *Electrochim. Acta*, 2001, **46**, 3517–3523.
10 F. Croce, A. D'Epifanio, J. Hassoun, A. Deptula, T. Olczac and B. Scrosati, *Electrochem. Solid-State Lett.*, 2002, **5**, A47.
11 A. Deb, U. Bergmann, E. J. Cairns and S. P. Cramer, *J. Synchrotron Radiat.*, 2004, **11**, 497–504.
12 A. Yamada, S. C. Chung and K. Hinokuma, *J. Electrochem. Soc.*, 2001, **148**, A224.
13 O. Haas, A. Deb, E. J. Cairns and A. Wokaun, *J. Electrochem. Soc.*, 2005, **152**, A191.
14 T. V. S. L. Satyavani, A. Srinivas Kumar and P. S. V. Subba Rao, *Eng. Sci. Technol. Int. J.*, 2016, **19**, 178–188.
15 J. Chen, S. Wang and M. S. Whittingham, *J. Power Sources*, 2007, **174**, 442–448.
16 L. He and Z. Zhao, *J. Alloys Compd.*, 2016, **688**, 386–391.
17 P. Axmann, C. Stinner, M. Wohlfahrt-Mehrens, A. Mauger, F. Gendron and C. M. Julien, *Chem. Mater.*, 2009, **21**, 1636–1644.
18 R. Amisse, M. Sougrati, L. Stievano, C. Davoisne, G. Dražič, B. Budič, R. Dominko and C. Masquelier, *Chem. Mater.*, 2015, **27**, 4261–4273.

19 H. Liu, M. J. Choe, R. A. Enrique, B. Orvañanos, L. Zhou, T. Liu, K. Thornton and C. P. Grey, *J. Phys. Chem. C*, 2017, **121**, 12025–12036.
20 S. Graulis, D. Chateigner, R. T. Downs, A. F. T. Yokochi, M. Quirós, L. Lutterotti, E. Manakova, J. Butkus, P. Moeck and P. Le Bail, *J. Appl. Crystallogr.*, 2009, **42**, 726–729.
21 A. A. Coelho, *J. Appl. Crystallogr.*, 2018, **51**, 210–218.
22 R. Dinnebier, A. Leineweber and J. Evans, *J. Rietveld refinement: practical powder diffraction pattern analysis using TOPAS*, 2018.
23 P. Thompson, D. E. Cox and J. B. Hastings, *J. Appl. Crystallogr.*, 1987, **20**, 79–83.
24 V. A. Streltsov, E. L. Belokoneva, V. G. Tsirelson and N. K. Hansen, *Acta Crystallogr., Sect. B: Struct. Sci.*, 1993, **49**, 147–153.
25 H. P. Gunnlaugsson, *Hyperfine Interact.*, 2016, **237**, 79.
26 Z. Li and I. SHINNO, *Mineral. J.*, 1997, **19**, 99–107.
27 B. Ravel and M. Newville, *J. Synchrotron Radiat.*, 2005, **12**, 537–541.
28 L. Tabassam, G. Giuli, A. Moretti, F. Nobili, R. Marassi, M. Minicucci, R. Gunnella, L. Olivi and A. Di Cicco, *J. Power Sources*, 2012, **213**, 287–295.
29 R. D. Shannon, *Acta Crystallogr., Sect. A: Cryst. Phys., Diffr., Theor. Gen. Crystallogr.*, 1976, **32**, 751–767.
30 H. Gao, L. Jiao, J. Yang, Z. Qi, Y. Wang and H. Yuan, *Electrochim. Acta*, 2013, **97**, 143–149.
31 G. Rousse, J. Rodriguez-Carvajal, S. Patoux and C. Masquelier, *Chem. Mater.*, 2003, **15**, 4082–4090.
32 A. S. Andersson, B. Kalska, L. Häggström and J. O. Thomas, *Solid State Ionics*, 2000, **130**, 41–52.
33 J. Chen and J. Graetz, *ACS Appl. Mater. Interfaces*, 2011, **3**, 1380–1384.
34 P. Gibot, M. Casas-Cabanas, L. Laffont, S. Levasseur, P. Carlach, S. Hamelet, J. M. Tarascon and C. Masquelier, *Nat. Mater.*, 2008, **7**, 741–747.
35 Z. Liu and X. Huang, *Solid State Ionics*, 2010, **181**, 907–913.
36 M. Maccario, L. Croguennec, A. Wattiaux, E. Suard, F. Le Cras and C. Delmas, *Solid State Ionics*, 2008, **179**, 2020–2026.
37 S. Hamelet, P. Gibot, M. Casas-Cabanas, D. Bonnin, C. P. Grey, J. Cabana, J. B. Leriche, J. Rodriguez-Carvajal, M. Courty, S. Levasseur, P. Carlach, M. Van Thournout, J. M. Tarascon and C. Masquelier, *J. Mater. Chem.*, 2009, **19**, 3979–3991.
38 A. A. M. Prince, S. Mylswamy, T. S. Chan, R. S. Liu, B. Hannoyer, M. Jean, C. H. Shen, S. M. Huang, J. F. Lee and G. X. Wang, *Solid State Commun.*, 2004, **132**, 455–458.
39 M. Wilke, F. Farges, P. E. Petit, G. E. Brown and F. Martin, *Am. Mineral.*, 2001, **86**, 714–730.
40 F. De Groot, G. Vankó and P. Glatzel, *J. Phys.: Condens. Matter*, 2009, **21**, 104207–104214.
41 T. E. Westre, P. Kennepohl, J. G. DeWitt, B. Hedman, K. O. Hodgson and E. I. Solomon, *J. Am. Chem. Soc.*, 1997, **119**, 6297–6314.
42 C. R. Randall, L. Shu, Y. M. Chiou, K. S. Hagen, M. Ito, M. Kitajima, R. J. Lachicotte, Y. Zang and L. Que, *Inorg. Chem.*, 1995, **34**, 1036–1039.
43 J. Wong, F. W. Lytle, R. P. Messmer and D. H. Maylotte, *Phys. Rev. B: Condens. Matter Mater. Phys.*, 1984, **30**, 5596–5610.
44 A. L. Roe, D. J. Schneider, R. J. Mayer, J. W. Pyrz, J. Widom and L. Que, *J. Am. Chem. Soc.*, 1984, **106**, 1676–1681.
45 C. Delacourt, P. Poizot, D. Bonnin and C. Masquelier, *J. Electrochem. Soc.*, 2009, **156**, A595.
46 N. Pailhé, A. Wattiaux, M. Gaudon and A. Demourgues, *J. Solid State Chem.*, 2008, **181**, 2697–2704.
47 J. Yano and V. K. Yachandra, *Photosynth. Res.*, 2009, **102**, 241–254.
48 G. R. Shulman, Y. Yafet, P. Eisenberger and W. E. Blumberg, *Proc. Natl. Acad. Sci. U. S. A.*, 1976, **73**, 1384–1388.
49 A. Deb, U. Bergmann, E. J. Cairns and S. P. Cramer, *J. Phys. Chem. B*, 2004, **108**, 7046–7051.
50 K. W. Nam, S. M. Bak, E. Hu, X. Yu, Y. Zhou, X. Wang, L. Wu, Y. Zhu, K. Y. Chung and X. Q. Yang, *Adv. Funct. Mater.*, 2013, **23**, 1047–1063.
51 S. I. Zabinsky, J. J. Rehr, A. Ankudinov, R. C. Albers and M. J. Eller, *Phys. Rev. B: Condens. Matter Mater. Phys.*, 1995, **52**, 2995–3009.
52 J. J. Rehr and A. L. Ankudinov, *J. Synchrotron Radiat.*, 2002, **10**, 43–45.
53 K. F. Hsu, S. K. Hu, C. H. Chen, M. Y. Cheng, S. Y. Tsay, T. C. Chou, H. S. Sheu, J. F. Lee and B. J. Hwang, *J. Power Sources*, 2009, **192**, 660–667.
54 M. Minicucci, L. Tabassam, R. Natali, G. Mancini, S. J. Rezvani and A. Di Cicco, *J. Mater. Sci.*, 2017, **52**, 4886–4893.
55 T. Zhao, W. Chu, H. Zhao, X. Liang, W. Xu, M. Yu, D. Xia and Z. Wu, *Nucl. Instrum. Methods Phys. Res., Sect. A*, 2010, **619**, 122–127.